Computers & Geosciences 54 (2013) 231–238

Contents lists available at SciVerse ScienceDirect

Computers & Geosciences

journal homepage: www.elsevier.com/locate/cageo

Quantitative discrimination between geological materials with variable density contrast by high resolution X-ray computed tomography: An example using amygdule size-distribution in ancient lava flows

Sanjoy M. Som [a,b,*], James W. Hagadorn [c], Weston A. Thelen [a,d], Alan R. Gillespie [a], David C. Catling [a], Roger Buick [a]

[a] Department of Earth and Space Sciences, University of Washington, Seattle, WA 98195, United States
[b] Blue Marble Space Institute of Science, Seattle, WA 98145, United States
[c] Department of Earth Sciences, Denver Museum of Nature & Science, Denver, CO 80205, United States
[d] Hawaii Volcano Observatory, Hawaii National Park, HI 96718, United States

ARTICLE INFO

Article history:
Received 28 June 2012
Received in revised form
15 November 2012
Accepted 17 November 2012
Available online 1 December 2012

Keywords:
X-ray tomography
Amygdules
Bubble-size distribution
Dynamic thresholding
Bootstrap resampling
Central limit theorem

ABSTRACT

The bubble-size distribution in 2.7 billion year old lava flows can be used as a proof of concept illustrating a new set of techniques for measuring volumes of geological materials with variable density contrasts using high-resolution X-ray computed tomography. Such studies have been limited in the past to high-contrast situations such as vesicles devoid of secondary fill. We present a new dynamic thresholding method for computationally separating amygdules from their basaltic matrix in X-ray images that is based on a technique used in seismology. The technique is sensitive to the gradient of the gray-scale value, rather than an absolute threshold value often applied to an entire set of X-ray images. Additionally, we present statistical methods for extrapolating the volumetric measurement mean and standard deviation of amygdules in the measured samples to the entire population in the flow. To do so, we create additional amygdule sample sets from the original sample set in the process of 'bootstrap' resampling, and use the Central Limit Theorem to calculate the mean and standard deviation of the amygdule population from these sample sets. This suite of methods allows the extension of bubble-size distribution studies typically done on modern flows to the ancient rock record and potentially has many other uses in geosciences where quantitative discrimination between materials with a range of densities is required.

1. Introduction

Measuring the dimensions (size, shape and relative abundance) of objects and spaces enclosed in solid substrates is critical for many geological investigations, including assessment of porphyroblasts in metamorphic rocks (Denison et al., 1997), fractures in sedimentary rocks (Hamblin, 1962), fluid flow through porous media (Coles et al., 1998) and vesicles in lava-flows (Sahagian et al., 2002) where large color, size or density contrasts allowed easy discrimination between the inclusions and their matrix. However in many geological settings inclusions of interest have variable contrast with the surrounding matrix owing to compositional differences. Under such circumstances it has often proved difficult to automate measurement of inclusions with much accuracy, so that truly quantitative dimensional determinations cannot be achieved. For applications like the one outlined below where high-quality measurements are required, new techniques for quantitative analysis are needed. We describe one such set of methods bringing together high-resolution X-ray computed tomography, image manipulation, a dynamic thresholding algorithm, and coupling bootstrap resampling to the Central Limit Theorem for determining the mean size and standard deviation of populations of gas bubbles filled in with secondary minerals (amygdules) in ancient lava flows. These techniques have other geological applications, especially where variable density contrast between inclusions and matrix is a problem. Possible examples include quantifying quartz and feldspar phenocrysts in intermediate to felsic igneous rocks (Gualda and Rivers, 2006), and distinguishing lapilli from cemented ash in pyroclastic flows.

Gas bubbles in lava flows are sensitive recorders of magmatic properties and Earth surface conditions, and their size distribution can be used to estimate gas loss from the flowing lava (Cashman et al., 1994). The degree of degassing is an important

* Correspondence to: Exobiology Branch, NASA Ames Research Center, Moffett Field, CA 94035, United States. Tel.: +1 650 604 1483.
E-mail address: sanjoy@uw.edu (S.M. Som).

0098-3004/$ - see front matter © 2012 Elsevier Ltd. All rights reserved.
http://dx.doi.org/10.1016/j.cageo.2012.11.019

control on surface morphological features, and thus emplacement style (Swanson and Fabbi, 1973). Furthermore, bubble-size distributions are also critical for understanding the thermal and rheological evolution of lavas (Aubele et al., 1988; Sahagian, 1985, Sahagian et al., 1989), and have been used as a paleoaltimetry proxy (Sahagian et al., 2002).

Bubble-size distribution studies have been limited to lava flows where the trapped bubbles are true voids (vesicles). Such voids enable measurement of bubble size distribution by several techniques, including (i) injection of plastic to fill the voids followed by rock dissolution in acid (Sahagian et al., 1989), (ii) stereology (Sahagian and Proussevitch, 1998; Toramaru, 1990), (iii) probability distribution functions (Mangan et al., 1993) and (iv) X-ray tomography (Sahagian et al., 2002; Song et al., 2001). High resolution X-ray computed tomography has emerged as the best tool because the density contrasts between void and rock are easily imaged, and it is less destructive and invasive than other methods (Ketcham and Carlson, 2001; Van Geet et al., 2000). Such studies have not yet been extended to lava flows in which the voids have been filled in by secondary minerals, typically quartz, calcite, chlorite or zeolites, because the density difference between void fill and host rock is not easily identified by automatic algorithms that rely on thresholding (i.e., on the absolute value of the returned pixel on the raw X-ray image; Ketcham (2005)). Such filled cavities (amygdules) typically characterize the vesicularity of more ancient lava flows that are often metasomatized or metamorphosed.

Here we present a suite of techniques to identify amygdules from X-ray images and compute errors automatically. Raw X-ray gray-scale images are processed through a low-pass Wiener–Kolmogorov filter prior to being treated using a modified seismological "picker" technique (Vanderkulk et al., 1965) to identify amygdules. Identification is followed by binarization and the resulting images are "cleaned" using image processing methods. This suit of techniques is applied to individual images, rather than defining detection parameters to an entire dataset. As such, this technique can accommodate subtle changes in instrumental X-ray intensity drift, and inherently has little sensitivity to the amygdule composition as long as a difference in density exists between the matrix and the secondary fill. The edge of scanned samples may suffer from a difference in returned intensity because of the shorter X-ray path length inside the sample, but this does not affect amygdule detection. The fully processed images are imported into BLOB3D (Ketcham, 2005), a freely available software product specifically designed for X-ray tomography that allows extraction of the dimensions of the amygdules.

The mean of the distribution and its error is often the quantity of interest. To characterize these parameters accurately, the fundamental assumption that the sample of the population characterized by the measured amygdules is a representative sample of the entire population of amygdules must be clearly expressed. Although seemingly straightforward, the clear statement of this assumption is a necessity for the statistics to be representative of the entire population of amygdules, rather than expressing the statistics of the measured sample alone. Indeed, this assumption allows the use of bootstrapping techniques to calculate the mean and the error in the mean of the entire population through application of the Central Limit Theorem.

2. X-ray imaging

X-ray imaging is based upon mapping the attenuation of X-rays as they travel through matter. X-rays are either photoelectrically absorbed or scattered via the Compton effect, resulting in a decrease in energy. Pair production, in which intensity is lost when the X-ray photons interact with the nucleus and are transformed into a positron-electron pair, is another attenuation physical process but only occurs at X-ray intensity >10 MeV (Ketcham and Carlson, 2001), substantially higher than the 100 keV used in this study. Photoelectric absorption and Compton scattering can be related to the linear attenuation coefficient of the sample scanned. Given the linear attenuation coefficient and sample thickness, the intensity of the X-ray arriving at a detector can be related to the initial intensity I_o through the Beer–Lambert law (Ketcham and Carlson, 2001). In practice, X-ray computed tomography relies on obtaining multiple intensity measurements of an object over a range of angular orientations, thus allowing 3D reconstruction of the object.

3. Sample description

The amygduloidal subaerial lava flows analyzed as a proof-of-concept in this study belong to the ~2.75 billion year old Bunjinah Formation in the Fortescue Group of the Pilbara Craton, Western Australia (Blake, 1993). Thin sections reveal a subophitic albite–chlorite–epidote–actinolite basaltic matrix of 0.2–0.5 mm crystals containing amygdules that are spheroidal and typically 1–6 mm in diameter (Fig. 1). They can be independent (Fig. 2A), partially coalesced, or fully coalesced with other amygdules (Fig. 2B). Partial coalescence is evident from the throat present between two amalgamating amygdules, whereas it is impossible to differentiate between a larger single amygdule and complete coalescence between two or more amygdules. The mineral fillings that characterize the amygdules vary in mineral composition and texture (Fig. 3) but consist dominantly of quartz and chlorite. Quartz crystal size in the amygdules can vary from 0.5 mm to microcrystalline, with the larger crystals typically located near the amygdule center. Quartz crystals <20 μm are dominantly equant and are concentrated toward the amygdule edge. Chlorite is also often observed as a mineral fill with an outer veneer of quartz, and typically occurs in larger amygdules (>2 mm). Microcrystalline quartz is the dominant secondary fill of both small and large amygdules. Discrete growth rings originating from nucleii within the amygdules can join to form composite mineral growth surfaces with alternating dark and bright bands (Fig. 2A).

Fig. 1. Amygdule-rich flow from the ~2.75 billion year old Fortescue Group, Pilbara Craton, Western Australia. Tip of pen (lower right) gives scale.

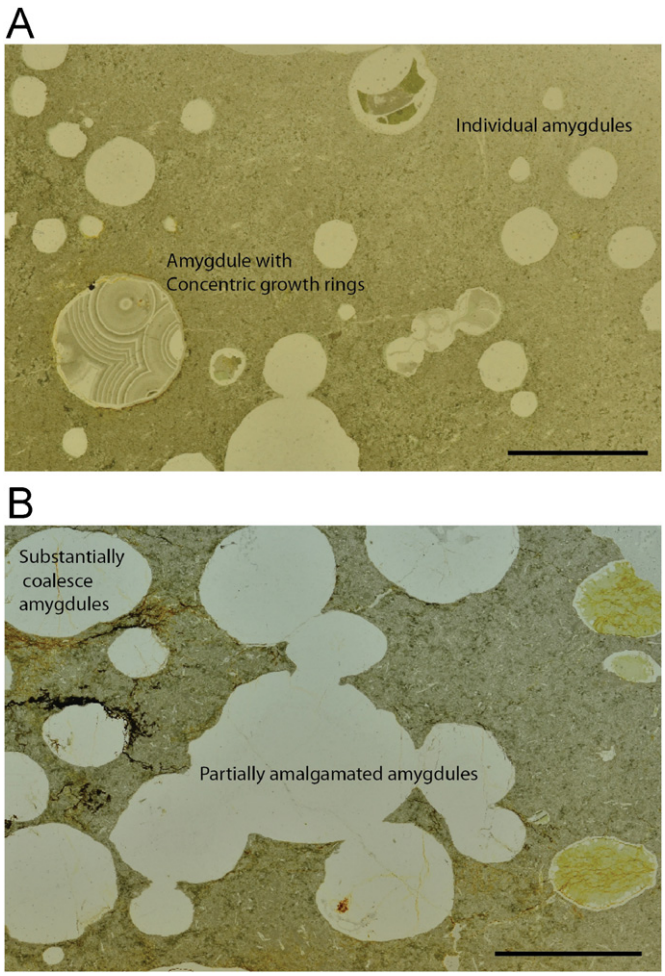

Fig. 2. Two thin sections of amygduloidal Fortescue basalt viewed in transmitted light, showing individual, partially coalesced, and substantially coalesced amygdules. Partial calescence is evident by the throat present between two joined amygdules. (A) Most amygdules are filled with secondary quartz and appear lighter than the basaltic matrix. Chlorite is the other dominant mineral and fills some darker amygdules. The large amygdule on the left with concentric growth rings is enlarged in Fig. 3E. (B) Large amalgamating amygdules also dominantly filled with secondary quartz. Two amygdules on the right-most side of the image have a secondary chlorite core with a thin quartz veneer (Fig. 2A). Both scale bars are 1 cm.

4. Methods

In this study, we used a bench-top Skyscan 1172 X-ray microtomography instrument. Cylindrical cores are typically preferred in tomography studies (Ketcham and Carlson, 2001) because they present a uniform cross-section to the X-rays when the cores rotate around their long axis inside the instrument. Bulk rock samples were drilled to produce 2.5 cm in diameter by ~3–4 cm tall cores using a water-lubricated diamond-grit hole saw that was mounted on a bench press.

Several parameters influence the quality of the X-ray images. Cores were scanned at a spatial scale of 0.03 mm per pixel, and an inter-slice spacing of 0.03 mm (leading to 0.03 mm^3 'voxels'—volume elements, or 3D pixels). The instrument was operated at 100 kV and 100 μA. The cores were scanned at 0.5° rotational intervals for 180°, where 3 frames were taken and averaged. The scans were divided into three horizontal sections because of the core height, with the instrument automatically adjusting the vertical position of the core for scanning. Each core took ~3 h to scan, and modified filtered back-projection that employed a cone-beam algorithm was used to convert the 360 projection images from each scan into 800–1300 horizontal X-ray slices per core.

In previous studies of gas bubbles in lavas (Sahagian et al., 2002; Song et al., 2001), the vesicles were air-filled voids (density, $\rho = \sim 1.23$ kg/m^3) contrasting sharply in density with the surrounding basaltic matrix ($\rho = \sim 2800$ kg/m^3) that translated into clear X-ray images of the vesicles. In this study, the vesicles are mineral-filled amygdules containing quartz ($\rho = \sim 2650$ kg/m^3) and chlorite ($\rho = 2700$–3300 kg/m^3). Thus, depending on secondary mineral fill, some amygdules appear brighter than the surrounding matrix, whereas others appear darker. In many image-processing protocols, a threshold algorithm is used to analyze images and separate the gray-scale values representing the amygdules from the matrix (Ketcham, 2005). However, in the analyses conducted here, imaging suffered instrument-related intensity drift which was manifested as progressively brighter images along a section of a core, with the next section starting darker and progressively getting brighter (Fig. 4). This drift made the use of a traditional threshold algorithm impractical, because the gray-scale value represented by a Digital Number (*DN*) between 0 (black) and 255 (white) identifying the threshold value of an amygdule at image *n*, would not be the same value at image $n+200$, for example. To overcome these difficulties, we developed a method based on gray-scale contrast existing at the boundary between an amygdule and the matrix (Fig. 5), rather than a single gray-scale threshold value applicable to all images. X-ray images (or "slices" as they are typically called; Fig. 6a) were imported into Matlab and first processed (taking advantage of Matlab's image analysis toolbox) using the "wiener2" function, an adaptive low-pass Wiener–Kolmogorov smoothing filter (Fig. 6b), which reduces noise by locally smoothing a zone of pixels (Lim, 1990). A structuring element (a "smoothing zone", in this case) of 10×10 pixels typically gave excellent results and is small enough to minimally affect the matrix–amygdule boundary.

A dynamic thresholding algorithm was developed and implemented to detect amygdules of variable density due to compositional differences. Had the amygdules been of homogeneous composition (or void vesicles) and the X-ray slices been affected by instrument drift alone, then the traditional means of normalizing the images with respect to each other would have been possible. Dynamic thresholding allows the detection of amygdules where both instrument drift and amygdule compositional variation applies. *DN* cross-sectional profiles of the images (5–15 per image depending on the anticipated amygdule density: Fig. 5) were taken (using Matlab's "improfile" function) and analyzed using an STA/LTA (Short-Term Amplitude/Long-Term Amplitude) "picker" algorithm used in seismology to detect earthquakes in a seismogram (Vanderkulk et al., 1965). This method scans through the cross-section *DN* values using two rectangular ("boxcar") averaging filters of different sizes (one 3 pixels long, the other 6 pixels long) and calculates the ratio between the averages (Fig. 5). We found that a ratio of 2 described well the location of a rapid change in gray-scale value (a "*DN* jump") corresponding to the edge of an amygdule. The *DNs* of the *N* pixels (DN_i) recorded between each *DN* jump are averaged into a mean, DN_j, as follows:

$$DN_j = \frac{1}{N}\sum_{i=1}^{N} DN_i \quad (1)$$

and represent the "*DN* threshold" of one amygdule *j*. Ignored are *DN* averages <30 (too dark and thus unlikely to be amygdules), and averages that occur over more than 200 pixels and less than 10 pixels between jumps (amygdules do not reach these dimensions in our samples). Averaging the *DN* averages (DN_j) for all *M* amygdules

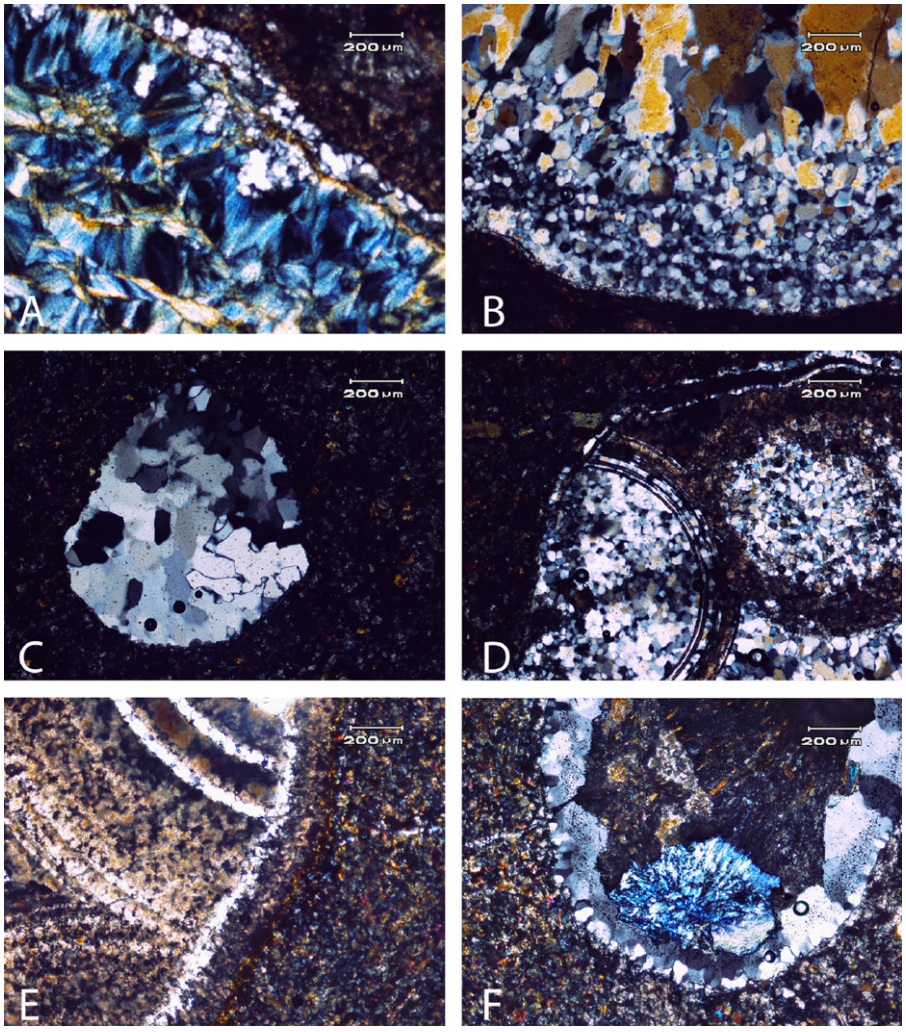

Fig. 3. Thin-section photomicrographs of amygdule fill; all images are under cross-polarized light. (A) Chlorite core in an amygdule. Basalt margin is at upper-right, and the amygdule is first rimmed with a thin quartz veneer. (B) Two-stage growth with small equant crystals on the outer edge of the amygdule (bottom of the image), and elongated large quartz grains at the core (top). (C) Equant to blocky quartz crystals filling the entire amygdule. (D) Multiple concentric growth rings of microcrystalline quartz, enveloping equant microquartz cores. (E) Two generations of concentric microcrystalline quartz growth rings filling amygdule (see Fig. 2A for context). (F) Amygdule filled with a veneer of fibrous microcrystalline quartz, surrounding blocky equant quartz crystals and a chlorite core.

detected in a slice yields a threshold value, DN_{slice}, (Fig. 5):

$$DN_{slice} = \frac{1}{M}\sum_{j=1}^{M} DN_j \tag{2}$$

Each set of images must be processed twice: once to detect amygdules darker than the matrix, and once to detect amygdules brighter than matrix. For dark/bright amygdules, the mean of the *DNs* between jumps (Eq. (1)) must be less/more than the mean of the *DNs* at the jumps. The first and last jump in a profile identifies the edge of the core (Fig. 5).

We found that the detection was improved by manually shifting the *DN* threshold value up or down by a multiple f (the value of which applied to all slices and depended on the core analyzed) of the standard deviation of DN_j.

$$DN_{slice} = DN_{slice} \pm f\sigma_{DN_j} \tag{3}$$

Each image is thus analyzed individually for the *DN* threshold that represents amygdules brightness independently of changes in intensity from the instrumentation. The selection of f is described below.

Binarization followed dynamic thresholding. Each image is binarized with"1" representing "amygdule" and "0" identifying "matrix" (Fig. 6c). These processes result in binarized images that are often speckled and contain the core boundary (Fig. 6c). The boundary is removed using a binary mask. Speckles (individual white pixels with binarized $DN=1$) are removed by 'morphological opening' (Gonzales and Woods, 2007), an image-processing technique (using Matlab's "imopen" function) that can be visualized as taking a structuring element (a disk with a radius of 2 pixels in our case) and sliding it inside the speckles (Fig. 6d). Because the structuring element is too large to fit inside the speckles, the speckles are removed and replaced by the black background values (with binarized $DN=0$). "Holes" in amygdules – volumes left unfilled by secondary mineralization – and rough edges on their outer surfaces are dealt with using 'morphological closing' (Gonzales and Woods, 2007), an image-processing technique (using Matlab's "imclose" function) that can be visualized as taking a structuring element (a disk with a radius of 5 pixels in our case) along the inside boundaries of the "hole" and along the outside of the amygdule. If the structuring element can touch any of the background ("0" pixels) without any part of the structuring element containing a pre-existing "1" pixel, then that background pixel remains so; if not, it is set to "1." Each slice goes through identical binarization. Fig. 6e shows a fully processed binarized image.

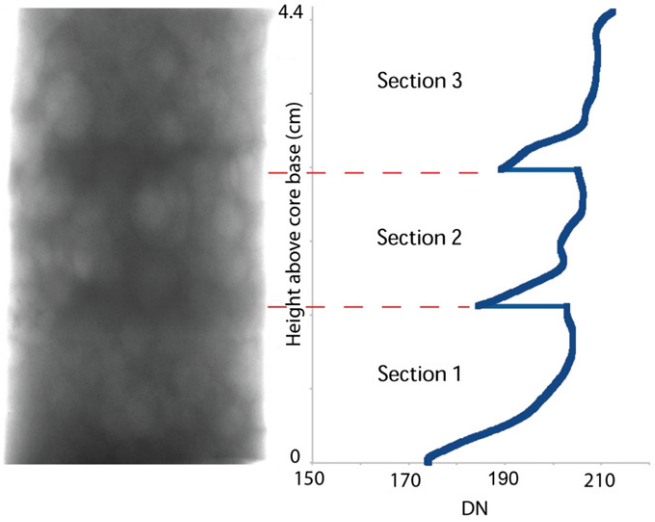

Fig. 4. Left: An X-ray transmission image of a 2.5 (D) × 4.4 (H) cm core, as obtained from the Skyscan HRXCT instrument. Scanning is separated into three sections to accommodate analysis of the tall specimen while maintaining relatively small voxel dimensions. The core is placed on the sample mount using putty (not shown), which allows easy manipulation to ensure that the core is parallel to the vertical spin axis of the mount, as the sample rotates during scan. Right: Digital Number (*DN*) representing mean slice intensity as a function of height. Notice that each section is darker at its base compared with its top. This prevents fixed thresholding for amygdule identification.

The analysis is done in three steps. In the first step, an image slice is randomly selected and the best factor f manually determined. In the second step, 6 images are randomly selected. This lets the user fine tune the factor f for optimal amygdule detection. In the third step, all images are automatically passed through the amygdule detection algorithm. The computer code used for this analysis is available from the main author upon request.

To obtain amygdule volume, binarized images are imported into BLOB3D (Ketcham, 2005), which is software made available by the University of Texas High-Resolution Computed Tomography facility. This program allows efficient and accurate identification and measurement of individual amygdules. As mentioned previously, the user inputs the pixel size (0.03 mm) and the inter-slice spacing (0.03 mm), so that each pixel now becomes a voxel of a known volume ($0.03 \times 0.03 \times 0.03$ mm). The software groups all the "1" voxels (i.e., the filled amygdules) and displays each resulting 'blob' to the user (Fig. 7a), who in the separation process (Ketcham, 2005) manually identifies blobs as relevant or not. Partially coalesced amygdules can be isolated with built-in tools available in BLOB3D and truncated or otherwise incomplete amygdules are discarded. Once selected, the number of voxels per blob is summed, yielding an amygdule volume. For 3 D visualization, the entire stack of binarized images can be imported into software such as ImageJ (free software made available by the NIH) and then animated (Fig. 7b).

We follow Proussevitch et al. (2007) and plot all measured amygdule volumes on semi-logarithmic scales as a histogram. The ideal number of histogram bins is calculated by the method of Scott (1979):

$$\text{Bin width} = 3.49\sigma n^{1/3} \tag{4}$$

where σ is the standard deviation of the dataset and n the total number of measured amygdules. Proussevitch et al. (2007) anticipate that bubble size distributions are commonly log-normal in linear space. It is thus useful to convert measurements to their logarithms because this converts the distribution of the dataset from log-normal to normal for conventional statistical analyses (Proussevitch et al., 2007). We test our data for normality by creating a normal quantile plot of the log of our data (Fig. 8 inset), and find a correlation coefficient of 0.9932, less than the critical correlation coefficient of 0.9976 (from NIST statistical tables) required to accept the null hypothesis that the data came from a normal distribution. In light of Fig. 2, this is expected, as some coalescence would cause the data to marginally deviate from normality. As such, the meaning of a standard deviation on the dataset alone becomes difficult unless an assumption of normality is put forward, in which case the standard deviation becomes the uncertainty in the mean. In contrast, applying two statistical techniques such as bootstrapping and the Central Limit Theorem that do not depend on the normality of the original dataset allows for the determination of the mean as well as the standard deviation. Furthermore, such statistics apply to the entire population, rather than the dataset alone (Davis, 2002).

5. Statistical analysis

If the transformed bubble-size distribution is normal, it may be fully described by its mean and standard deviation. Sahagian et al. (2002) obtained a modal vesicle-size from a histogram composed of "dozens of bins; thousands of vesicles" (Sahagian et al., 2002), and calculated an uncertainty in volume of $<2\%$ based on a specific vesicle dimension (1000 μm). A more thorough statistical analysis is used here in which the total range of vesicle volumes accurately measured is taken into account to calculate the uncertainty in the mean volume, rather than focusing on the uncertainty of a specific dimension. More importantly, this method allows the statistics of the entire population of amygdules to be synthesized, as the amygdule volumes obtained using HRXCT represent only a sample of the much larger population of amygdules within each lava flow.

We assume that the samples are representative of the population of amygdules. This is necessary in order to extend the statistical results from the sample to the entire population. We use a resampling technique called the 'bootstrap' (Efron, 1979), in which a new dataset is created numerically by randomly picking amygdule volumes from the original HRXCT-obtained dataset. After an amygdule is picked from the original dataset, it is copied and returned to the original sample set. As such, the next randomly picked amygdule will come from the exact same dataset as the one previously picked from. This is repeated until the new dataset has the same number of elements as the original one. This whole process is then repeated 999 times to create $N=1000$ different datasets, all derived from the original one. Because the original dataset is in effect a random sample from the population, each randomly obtained dataset acquired from the original random one also is a random sample from the population. The Central Limit Theorem states that the mean of randomly obtained samples from an original dataset (whether normally distributed or not) taken randomly from a population will be normally distributed, and the mean of this distribution of means will be equal to the population mean, usually denoted μ (Davis, 2002). Furthermore, if each dataset has the same standard deviation σ as the original dataset, then the error about the mean σ_μ may be obtained using (Bevington, 1969):

$$\sigma_\mu = \sigma/N^{1/2} \tag{5}$$

where N is the number of datasets.

However, if the uncertainties in each dataset are *not* equal, the error about the mean σ_μ is obtained with:

$$\sigma_\mu = \{1/(\Sigma(1/\sigma_i{}^2))\}^{1/2} \tag{6}$$

Eq. (6) reverts back to Eq. (5) if σ_i's are identical. The size of σ_μ can also inform us about the quality of the original HRXCT-obtained sample. If outliers exist, one would expect a larger σ_μ compared

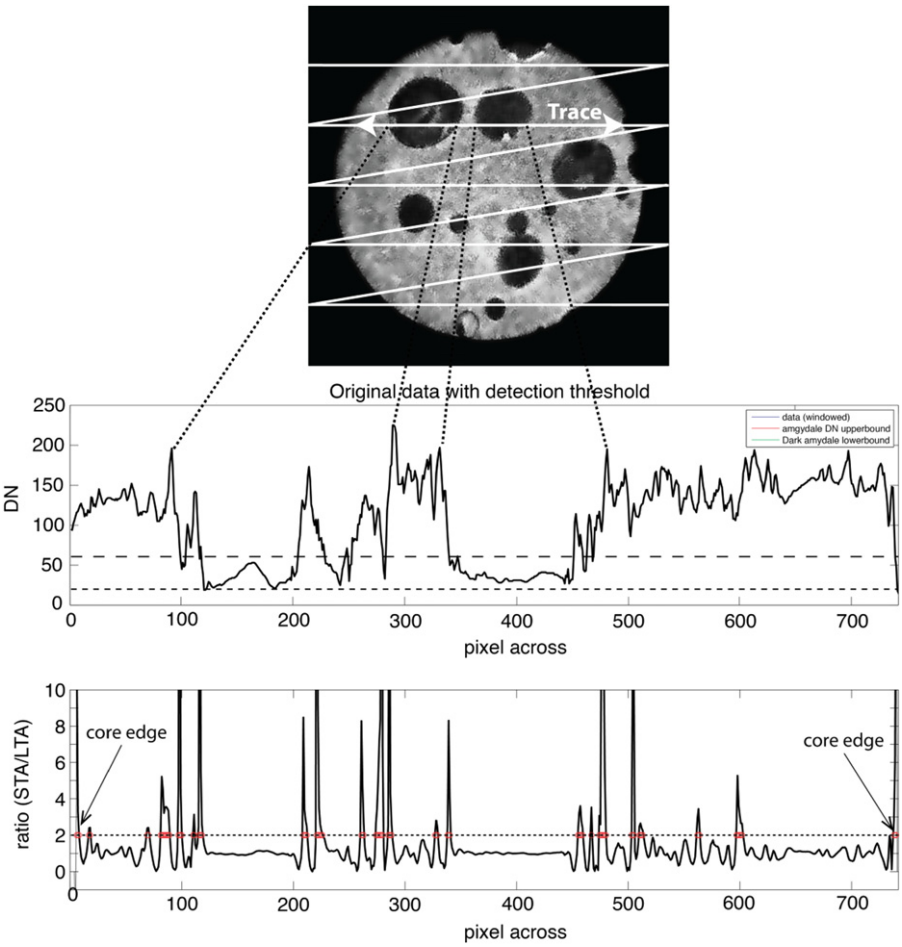

Fig. 5. Upper: An X-ray image of a slice with the location of the cross-sections used for dynamic thresholding indicated by the horizontal and diagonal lines. Amygdules are visible as dark circles and ovals. The white arrows show a trace that is mapped on graphs below. Middle: The digital number (*DN*) values corresponding to the arrowed trace in the upper panel serving as an example of one horizontal trace. Lower: the corresponding STA/LTA function. The dotted horizontal line represents our threshold value of 2 where a sharp change in *DN* intensity occurs (see text for details). The first and last detections correspond to the core edge.

with less scattered data. To compute the standard error in amygdule volume measurement S_{Vm} applicable to the population, we need to back-transform the results to linear space. Let $\log(V_{\mathrm{m}})=\mu$, where V_{m} is the population mean in linear space, from which:

$$V_{\mathrm{m}} = 10^{\mu} \tag{7}$$

The most probable error S_{Vm} in V_{m} due to the error σ_{μ} in σ is the square root of the variance:

$$S_{\mathrm{Vm}} = \{[(\partial V_{\mathrm{m}}/\partial\mu)\sigma_{\mu}]^2\}^{1/2} \tag{8}$$

The term $(\partial V_{\mathrm{m}}/\partial\mu)$ can be written as $10^{\mu}\ln(10)$ from the relationship:

$$\partial a^{\mathrm{x}}/\partial x = \mathrm{a}^{\mathrm{x}}\ln(a) \tag{9}$$

where a is a constant and x is a generic independent variable. Therefore, the volumetric error in the mean is expressed as:

$$S_{\mathrm{Vm}} = \{10^{\mu}\ln(10)\sigma_{\mu}\}^{1/2}. \tag{10}$$

Our goal with these samples from the upper vesicular zone of an Archean lava flow was to illustrate the dynamic thresholding algorithm. A complete characterization of the vesicularity of a lava flow would be beyond the analysis presented here. This would include the vertical size distribution of amygdules within the flow, amygdule-size distribution analyses in the lower vesicular zone (Aubele et al., 1988), and additional mathematical treatments to fully characterize the distribution (e.g., Proussevitch et al., 2007; Kaplan, 1999; Shapiro and Wilk, 1965).

6. Results

The results of our proof-of-concept study are plotted in Fig. 8. We find, after measuring 885 separate amygdules, a mean sample amygdule volume of $2.24 \pm 2.01\ \mathrm{mm}^3$, from which the mean population amygdule volume can be found to be $2.25 \pm 0.066\ \mathrm{mm}^3$ equivalent to 1.6 ± 0.5 mm in diameter by coupling bootstrap resampling to the Central Limit Theorem. This value for an Archean lava flow compares well with measurements of vesicle size in upper vesicular zones of modern flows. Sahagian et al. (2002) found modal diameters in the range 1.22–1.68 mm in nine basaltic lava flows in Hawaii, and Aubele et al. (1988) measured vesicles of 2.5 ± 1.27 mm 20 cm below another Hawaiian flow top.

7. Conclusion

The bubble-size distribution in a 2.7 billion year old amygduloidal lava flow was used as a proof of concept to illustrate a new set of techniques for measuring volumes of geological materials with low density contrast to their matrix using high resolution

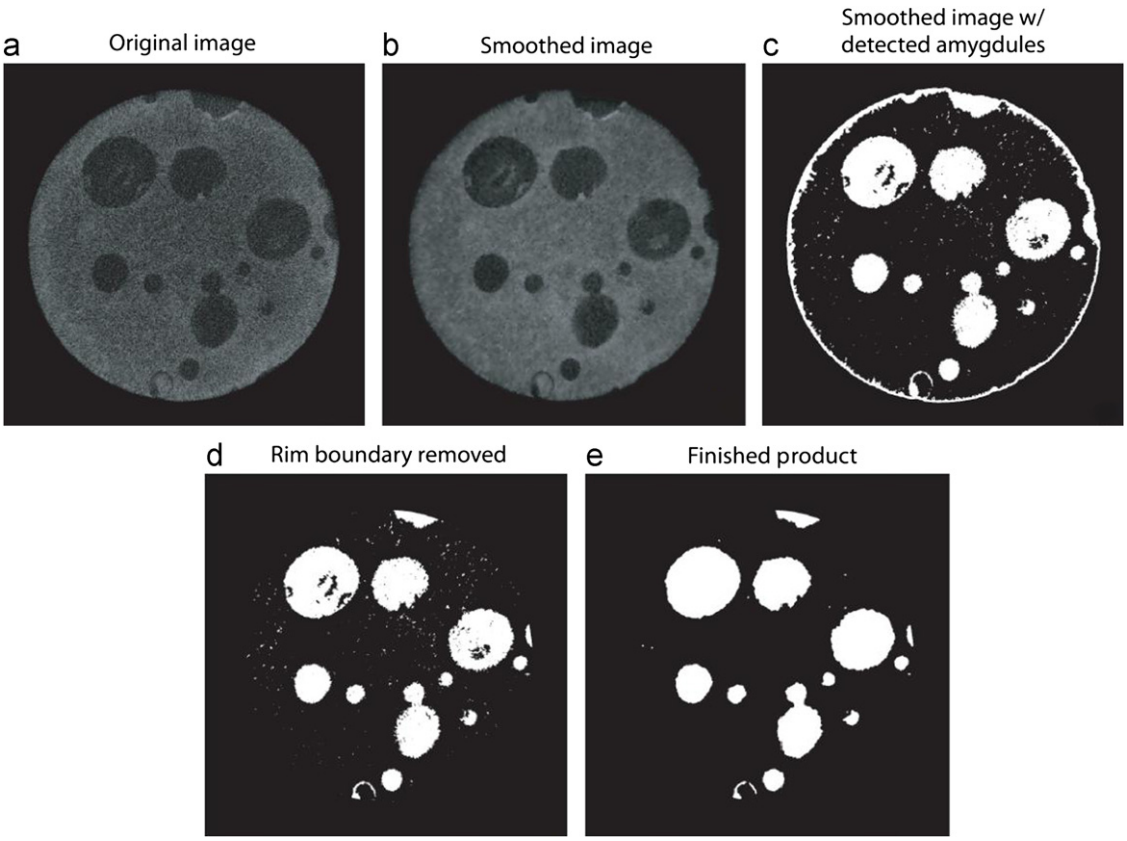

Fig. 6. Image-analysis procedure. (a) Original cross-sectional image as obtained from HRXCT, (b) Image smoothed using a low-pass Wiener–Kolmogorov filter, (c) Binarization, (d) Core boundary removed, (e) Fully processed image following morphological erosion to remove the speckles, and morphological closing to fill holes and smooth edges.

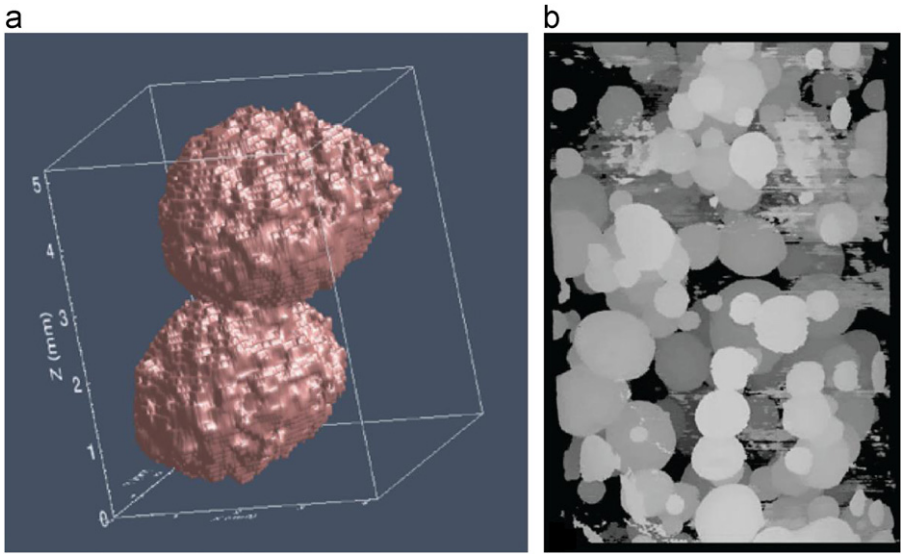

Fig. 7. Example of amygdule rendering. (a) These two touching amygdules imaged in BLOB3D can be manually separated using the software. (b) The entire stack of binarized images forming a complete core as visualized using the ImageJ software.

X-ray computed tomography. The size distribution of vesicles in lava flows is of particular interest because it can be used to estimate gas loss of flowing lava, and to model the thermal and rheological evolution of these lavas. Such studies have not previously been extended to ancient lava flows because secondary minerals fill in the vesicle void, forming amygdules of variable density compared with their rock matrix. We use statistical methods involving 'bootstrap' resampling, coupled with the Central Limit Theorem to extend the bubble-size distribution results to the entire population of amygdules, rather than to the sample alone. This X-ray technique is not limited to our particular application, but could be used in other circumstances where variable density contrasts between subject and background limit the ability to quantitatively differentiate the two.

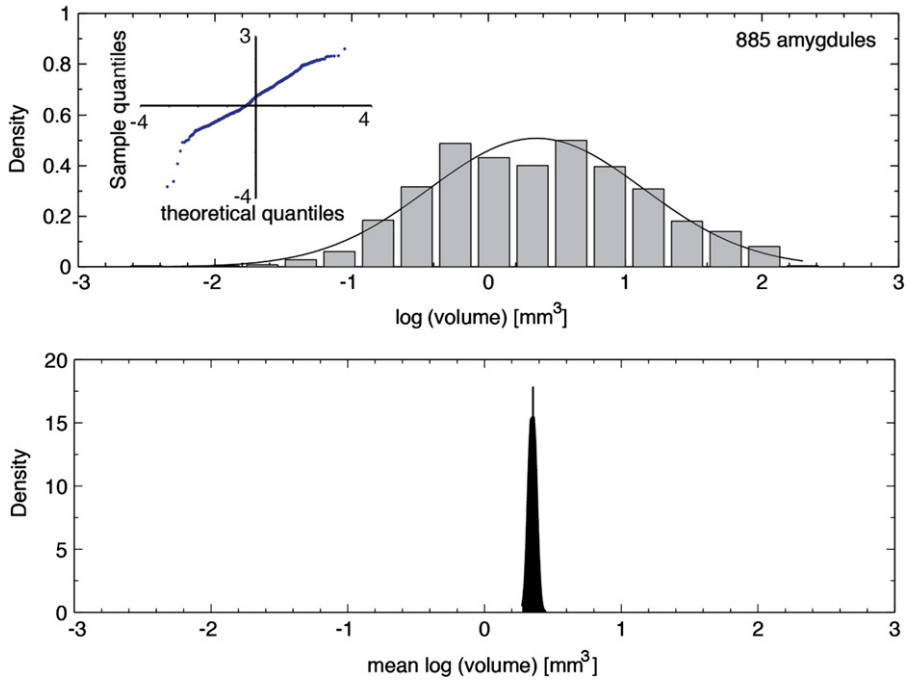

Fig. 8. Results of analysis of this proof-of-concept study, for amygdules from the flow top. (A) The logarithmic distribution of the amygdule volume spreads over several orders of magnitude in a quasi-normal distribution, yielding a mean amygdule size of 2.24 ± 2.01 mm^3. Inset: normal quantile plot of amygdule volumes. The correlation coefficient $r=0.9932$ is less than the critical r value of 0.9976 required to accept the null hypothesis that the data came from a normal distribution (B) Distribution of the mean of 1000 datasets analyzed using bootstrapping techniques. The mean of the means of the sample datasets (2.25 mm^3) is the mean of the population, and the standard deviation of this distribution is the error in the mean of the population of amygdules (0.066 mm^3).

Acknowledgements

This work was funded by NASA Exobiology/Astrobiology grant NNX08AP56G. The help of John Perreault is gratefully acknowledged in assisting with BLOB3D amygdule extraction. Richard Ketcham and Philip Watson at the UT HRXCT facility are thanked for their helpful feedback during our implementation of BLOB3D. This manuscript benefited from constructive reviews by Richard Ketcham and Guilherme Gualda.

References

Aubele, J.C., Crumpler, L.S., Elston, W.E., 1988. Vesicle zonation and vertical structure of basalt flows. Journal of Volcanology and Geothermal Research 35, 349–374.

Bevington, P.R., 1969. Data reduction and Error Analysis for the Physical Sciences. McGraw-Hill, NY 338 p.

Blake, T.S., 1993. Late Archaean crustal extension, sedimentary basin formation, flood basalt volcanism and continental rifting: the Nullagine and Mount Jope Supersequences, Western Australia. Precambrian Research 60, 185–241.

Cashman, K.V., Mangan, M.T., Newman, S., 1994. Surface degassing and modifications to vesicle size distribution in active basalt flows. Journal of Volcanological and Geothermal Research 61, 45–68.

Coles, M.E., et al., 1998. Developments in Synchrotron X-ray microtomography with applications to flow in porous media. SPE Reservoir Evaluation and Engineering 1, 288–296.

Davis, J.C., 2002. Statistics and Data Analysis in Geology. Wiley, NY 550 p.

Denison, C., Carlson, W.D., Ketcham, R.A., 1997. Three-dimensional quantitative textural analysis of metamorphic rocks using high-resolution computed X-ray tomography: Part I. Methods and techniques. Journal of Metamorphic Petrology 15, 29–44.

Efron, B., 1979. Bootstrap methods: another look at the jackknife. The Annals of Statistics 7, 1–26.

Gonzales, R.C., Woods, R.E., 2007. Digital Image Processing, third ed. Prentice Hall.

Gualda, G.A.R., Rivers, M., 2006. Quantitative 3D petrography using X-ray tomography: application to Bishop Tuff pumice clasts. Journal of Volcanology and Geothermal Research 154, 48–62.

Hamblin, W.K., 1962. X-ray radiography in the study of structures in homogeneous sediments. Journal of Sedimentary Petrology 32, 201–210.

Kaplan, D.T., 1999. Resampling Stats in MATLAB. Resampling Stats, Inc., Arlington, VA 1999.

Ketcham, R.A., 2005. Computational methods for quantitative analysis of three-dimensional features in geological specimens. Geosphere 1, 32–41.

Ketcham, R.A., Carlson, W.D., 2001. Acquisition, optimization and interpretation, of X-ray computed tomographic imagery: applications to the geosciences. Computers & Geosciences 27, 381–400.

Lim, J.S., 1990. Two-Dimensional Signal and Image Processing. Prentice-Hall, NJ 548p.

Mangan, M.T., Cashman, K.V., Newman, S., 1993. Vesiculation of basaltic magma during eruption. Geology 21, 157–160.

Proussevitch, A.A., Sahagian, D.L., Tsentalovich, E.P., 2007. Statistical analysis of bubble and crystal size distributions: formulations and procedures. Journal of Volcanological and Geothermal Research 164, 95–111.

Sahagian, D.L., 1985. Bubble migration and coalescence during the solidification of basaltic lava flows. Journal of Geology 93, 205–211.

Sahagian, D.L., Anderson, A.T., Ward, B., 1989. Bubble coalescence in basalt flows: comparison of a numerical model with natural examples. Bulletin of Volcanology 52, 49–56.

Sahagian, D.L., Proussevitch, A.A., 1998. 3D particle size distributions from 2D observations: stereology for natural applications. Journal of Volcanology and Geothermal Research 84, 173–196.

Sahagian, D.L., Proussevitch, A.A., Carlson, W.D., 2002. Analysis of vesicular basalts and lava emplacement processes for application as a paleobarometer/paleoaltimeter. Journal of Geology 110, 671–685.

Scott, D.W., 1979. On optimal and data-based histograms. Biometrika 66 (3), 605.

Shapiro, S.S., Wilk, M.B., 1965. An analysis of variance test for normality (complete samples). Biometrika 52, 591–611.

Song, S.R., Jones, K.W., Lindquist, B.W., Dowd, B.A., Sahagian, D.L., 2001. Synchrotron X-ray computed microtomography: studies on vesiculated basaltic rocks. Bulletin of Volcanology 63, 252–263.

Swanson, D.A., Fabbi, B.P., 1973. Loss of volatiles during fountaining and flowage of basaltic lava at Kilauea volcano. Hawaii.Journal of Research of the US Geolological Survey 1, 649–658.

Toramaru, A., 1990. Measurement of bubble size distribution in vesiculated rocks with implications for quantitative estimation of eruption processes. Journal of Volcanology and Geothermal Research 43, 71–90.

Vanderkulk, W., Rosen, F., Lorenz, S. 1965. Large Aperture Seismic Array Signal Processing Study, IBM Final Report, ARPA Contract Number SD-296.

Van Geet, M., Swennen, R., Wevers, M., 2000. Quantitative analysis of reservoir rocks by microfocus X-ray computerised tomography. Sedimentary Geology 132, 25–36.